

Article

Heat Transfer Investigation in Plus-Shaped Enclosure Using Power Law Fluid: A Finite Element Approach

Imran Shabir Chuhan ¹, Jing Li ^{1,*} , Ziyu Guo ¹, Muhammad Yaqub ² and Malik Abdul Manan ²

¹ Interdisciplinary Research Institute, Faculty of Science, Beijing University of Technology, Beijing 100124, China; imranshabbir1989@hotmail.com (I.S.C.); guozy666@126.com (Z.G.)

² Faculty of Information Technology, Beijing University of Technology, Beijing 100124, China; myaqubciitswl@gmail.com (M.Y.); manansandila@yahoo.com (M.A.M.)

* Correspondence: leejing@bjut.edu.cn

Abstract: The main purpose of this study is to investigate the thermal behavior of power law fluid within a plus-shaped cavity under the influence of natural convection, also taking into account the Darcy number and magnetohydrodynamics (MHD). The problem is formulated as a system of partial differential equations considering the power law fluid's rheological behavior. The left-side walls are maintained at a specific low temperature while the lower and the right-side walls have uniform maximum temperatures. The boundary condition is designed to enhance heat transfer efficiency within the cavity, utilizing advanced thermal insulation methodologies. Finite element method (FEM) simulations are conducted, and a grid independence test is performed to validate the results. The impact of relevant parameters on the variation in momentum and thermal distributions is investigated using streamline and isothermal contour plots. The results indicate that as the Rayleigh number increases, the kinetic energy also increases, whereas the viscosity and circulation zones expand with an increase in the power law index. The Nusselt number exhibits a higher value in the shear-thinning case ($n = 0.7$) compared to the Newtonian ($n = 1$) and shear-thickening ($n = 1.2$) cases. This empirical observation underscores the vital role that fluid rheology plays in molding the overall heat transfer performance within the cavity. The study concludes that there is a distinct correlation between the heat transfer rate and the Rayleigh number (Ra). As Ra increases, there is a significant improvement in the heat transfer rate within the flow domain. Furthermore, the fluid behavior and heat transfer performance within the cavity are significantly influenced by the presence of magnetohydrodynamics (MHD) and the Darcy effect.

Keywords: natural convection; power law; finite element method; plus-shape enclosure; heat transfer; MHD



Citation: Chuhan, I.S.; Li, J.; Guo, Z.; Yaqub, M.; Manan, M.A. Heat Transfer Investigation in Plus-Shaped Enclosure Using Power Law Fluid: A Finite Element Approach. *Appl. Sci.* **2023**, *13*, 11042. <https://doi.org/10.3390/app131911042>

Academic Editor: Luis Lugo

Received: 30 August 2023

Revised: 25 September 2023

Accepted: 26 September 2023

Published: 7 October 2023



Copyright: © 2023 by the authors. Licensee MDPI, Basel, Switzerland. This article is an open access article distributed under the terms and conditions of the Creative Commons Attribution (CC BY) license (<https://creativecommons.org/licenses/by/4.0/>).

1. Introduction

Over the past decade, the study of natural convection has garnered significant attention from researchers across various disciplines. Its ability to transfer heat without external energy sources makes natural convection a promising area of research for numerous natural and industrial applications. From energy-efficient cooling systems to advanced heat exchangers, the potential for natural convection to revolutionize engineering practices is immense. Numerous investigations have explored the natural convection that arises when a solitary heated object is positioned within an enclosure where the walls are maintained at lower temperatures [1–6]. However, in practical engineering applications, it becomes essential to gain insights into temperature gradients and fluid flow within enclosures that consist of multiple objects arranged in diverse positions. Studying the convective transport driven by buoyancy within enclosures holds significant importance due to its wide range of applications, including energy storage, material processing, cooling systems, and human comfort. Ostrach [7] conducted a comprehensive examination of heat transfer in natural

convective flow, wherein the majority of recent research has concentrated on scenarios featuring either horizontal or vertical temperature gradients. Natural convection through enclosures with partially active walls, such as heated and cooled walls, can be used for cooling electrical gadgets and buildings [8]. Using the asymptotic approach, Kwon et al. [9] developed a new heat transfer coefficient correlation for radial plate-fin heat sinks and thermal optimized horizontally oriented ones using natural convection. Schaub et al. [10] developed an analytical method for predicting heat transmission via unsteady natural convection. Using an analytical solution, Ahn et al. [11] determined the conditions under which free convection occurs in vertically asymmetrically heated shafts at low Rayleigh numbers. Malkeson et al. [12] and Aloui et al. [13] analyzed the onset of Rayleigh-Bernard convection. The focus of the study is the investigation of power law fluid convection in rectangular-shaped cavities. Specifically, the study examines the convection patterns in an enclosure with differentially heated walls, where the lower wall is heated while the side walls are adiabatic.

Polymeric fluids with shear-thinning and -thickening properties have practical applications. Their viscosity changes with shear rate, making coupling momentum and thermal fields crucial in measuring heat transfer. These fluids significantly minimize heat loss in various applications, including storage tanks, crude oil production, food reheating, electronic component cooling, and polymeric pallet melting or heating. A mathematical model called the power law model provides a comprehensive approach to understanding these materials. The power law model is a significant tool for predicting the behavior of polymeric materials under both minimum and maximum stresses and accurately describing the deformation rate response. Various studies have extensively investigated the behavior of power law materials within confined geometries accompanied by natural convection. Khezzar et al. [14] utilized the Boussinesq approximation to demonstrate the characteristics of a power law fluid with variable density in a 2D enclosure subject to different Rayleigh numbers. Sairamu and Chhabra [15] investigated the behavior of thermal-dependent density and quiescent power law fluid enclosed in an inclined cavity subjected to laminar flow for different kinematic conditions. In their study, Mishra and Chhabra [16] investigated the laminar convective motion of a power law fluid through a series of horizontally aligned tandem cylinders with differential heating. In their study, Hamza et al. [17] discussed entropy generation analysis using a hybrid nanofluid model in a convectively heated moving wedge. References [18–24] provide a comprehensive of recent advancements concerning power law non-Newtonian fluids, encompassing diverse physical aspects and various flow-generating domains.

Several investigations have concentrated on the heat transfer performance of Newtonian fluids in trapezoidal cavities, where mixed convection and natural have been investigated for magnetohydrodynamic (MHD) flows. Pirmohammadi and Ghassemi [25] examined the impact of a magnetic field on the heat transfer of laminar natural convective in a titled cavity and maximum temperature at the lower side. They found that a higher Hartmann number reduces convective heat transfer for a given inclination. In recent years, various research has examined natural convection under inclined magnetic fields [26–28]. Sheremet et al. [29] thoroughly investigated the MHD heat convection in a wavy enclosure with a porous medium, and the lower wall has a maximum temperature. Numerous researchers have examined the impact of incorporating porous media within an enclosure for various purposes, as porous materials can enhance or reduce heat transfer [30–32]. The flow within a vertical cavity with a wavy shape that was permeated by a porous medium was examined by Aydin et al. [33]. They obtained a numerical solution using the finite element method. Rizwan et al. [34] established a complete structure for the heat transfer effects of free convection in a porous corrugated cavity under MHD flow and a uniform magnetic field, utilizing a properly non-dimensional system that was solved through FEM with high resolution near the surface of corrugation, and presented visualizations of flow patterns and temperature distribution for various parameters. This includes the process of discretizing the governing partial differential equations through a weak formulation. The weak form

permits the utilization of lower-degree polynomials for approximating field variables. The weak form for non-Newtonian fluids was introduced by [35,36]. Subsequently, Baranovskii et al. [37] discussed the optimal control problem associated with a mathematical model that describes the steady flow of a nonlinear-viscous, incompressible fluid within a bounded two-dimensional domain. Weak solutions are constructed to minimize a specified cost functional, subject to a given bounded set of permissible controls.

This article investigates the heat transfer effects in a porous cross-shaped cavity under MHD flow and a uniform magnetic field. The research will be conducted through a comprehensive literature review on the subject. Subsequently, a mathematical model has been developed to capture and describe the occurrence of free convection within the cavity. This article explores the non-Newtonian model characterizing shear-thinning and shear-thickening fluid behaviors within a plus-shaped enclosure. The study seeks to elucidate the influence of various factors, encompassing the Reynolds number, magnetic field inclination, the Hartmann number, and power law index. Numerical simulations were then performed to solve the governing partial differential equations using the finite element method, which provides detailed insights into the flow patterns and thermal distribution within the cavity. Graphical results such as streamlines and isotherms were presented to aid in visualizing the simulation outcomes. Finally, based on the results obtained, a conclusion was drawn, which summarized the findings and implications of the study.

2. Mathematical Model

Consider a 2D steady-state free convective power law fluid flow with constant density in a plus-shaped cavity. The enclosure is enclosed by vertical walls maintained at constant temperatures, with the right-side lower wall uniformly heated while the left-side upper wall has low temperature. The enclosure is assumed to be impermeable, with no movement of the walls. Therefore, this paper introduces originality in investigating the non-Newtonian model that characterizes the behaviors of shear-thinning and shear-thickening fluids. The Boussinesq assumption has been implemented, and the influence of Rayleigh dissipation is considered negligible. The illustration in Figure 1 depicts the physical layout of the problem.

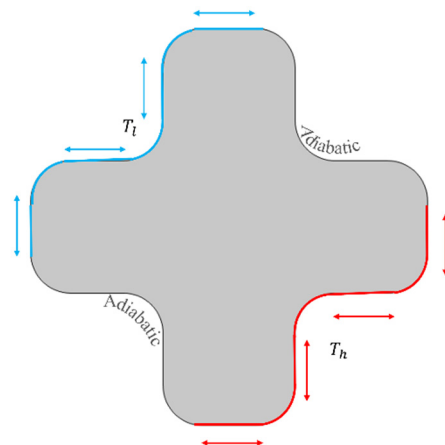


Figure 1. Schematic diagram representing the problem.

Considering the above assumptions, we utilize the following governing equations to represent the flow phenomenon [38–41]

$$\frac{\partial u}{\partial x} + \frac{\partial v}{\partial y} = 0 \quad (1)$$

$$u \frac{\partial u}{\partial x} + v \frac{\partial u}{\partial y} = -\frac{1}{\rho} \frac{\partial p}{\partial x} + \frac{1}{\rho} \left(\frac{\partial \tau_{xx}}{\partial x} + \frac{\partial \tau_{xy}}{\partial y} \right) + \zeta_x \quad (2)$$

$$u \frac{\partial v}{\partial x} + v \frac{\partial v}{\partial y} = -\frac{1}{\rho} \frac{\partial p}{\partial y} + \frac{1}{\rho} \left(\frac{\partial \tau_{xy}}{\partial x} + \frac{\partial \tau_{yy}}{\partial y} \right) + \xi_y \tag{3}$$

where $(\rho, \mu, \xi_x, \xi_y)$ are fluid density, kinematic viscosity, and force terms (magnetic field and Boussinesq approximation). The force includes thermal diffusivity ρ and solutal expansions (β_T, β_c) .

$$(\xi_x, \xi_y) = \left(\rho B_0^2 \left(v \sin \gamma \cos \gamma - u \sin^2 \gamma \right) - \frac{\mu}{K} u, \rho B_0^2 \left(u \cos \gamma \sin \gamma - v \cos^2 \gamma \right) - \frac{\mu}{K} v + \rho g [\beta_c (c - c_l) + \beta_T (T - T_l)] \right)$$

$$u \frac{\partial T}{\partial x} + v \frac{\partial T}{\partial y} = \varsigma \left(\frac{\partial^2 T}{\partial x^2} + \frac{\partial^2 T}{\partial y^2} \right) \tag{4}$$

$$u \frac{\partial c}{\partial x} + v \frac{\partial c}{\partial y} = D \left(\frac{\partial^2 c}{\partial x^2} + \frac{\partial^2 c}{\partial y^2} \right) \tag{5}$$

$$\tau_{ij} = 2\mu_a D_{ij} = \mu_a \left(\frac{\partial u_i}{\partial x_j} + \frac{\partial u_j}{\partial x_i} \right)$$

$$\mu_a = K \left\{ 2 \left[\left(\frac{\partial u}{\partial x} \right)^2 + \left(\frac{\partial v}{\partial y} \right)^2 \right] + \left(\frac{\partial v}{\partial x} + \frac{\partial u}{\partial y} \right)^2 \right\}^{\frac{n-1}{2}}$$

D is magnetic diffusivity and ς is the diffusion coefficient.

The non-dimensional forms of Equations (1)–(5) are obtained by using dimensionless parameters as

$$X = \frac{x}{L}, Y = \frac{y}{L}, U = \frac{uL}{\alpha}, V = \frac{vL}{\alpha}, (T_h - T_l)\theta = (T - T_l), P_r \rho \alpha^2 = p.L^2, Da = \frac{K}{L^2}$$

$$P_r = \frac{K L^{2-2n}}{\rho \alpha^{2-n}}, (c_h - c_l).C = (c - c_l), Ra = \frac{\rho \beta_T g L^{2n+1} \Delta T}{K \alpha^n}, Le = \frac{\varsigma}{D}, Ha = BH \sqrt{\frac{\rho}{\mu}} \tag{6}$$

The boundary conditions are created by inserting Equation (6) into (1)–(5), as follows.

$$\frac{\partial U}{\partial X} + \frac{\partial V}{\partial Y} = 0 \tag{7}$$

$$U \frac{\partial U}{\partial X} + V \frac{\partial U}{\partial Y} = -\frac{\partial P}{\partial X} + P_r \left[2 \frac{\partial}{\partial X} \left(\bar{\mu}_a \frac{\partial U}{\partial X} \right) + \frac{\partial}{\partial Y} \left(\bar{\mu}_a \left(\frac{\partial U}{\partial Y} + \frac{\partial V}{\partial X} \right) \right) \right] + \xi_X, \tag{8}$$

$$U \frac{\partial V}{\partial X} + V \frac{\partial V}{\partial Y} = -\frac{\partial P}{\partial Y} + P_r \left[2 \frac{\partial}{\partial Y} \left(\bar{\mu}_a \frac{\partial V}{\partial Y} \right) + \frac{\partial}{\partial X} \left(\bar{\mu}_a \left(\frac{\partial U}{\partial Y} + \frac{\partial V}{\partial X} \right) \right) \right] + \xi_X, \tag{9}$$

$$(\xi_X, \xi_Y) = \left(Ha^2 P_r \left(\sin \gamma \cos \gamma V - \sin^2 \gamma U \right) - \frac{P_r}{Da} U, Ha^2 P_r \left(\sin \gamma \cos \gamma U - \cos^2 \gamma V \right) - \frac{P_r}{Da} V + P_r Ra (NC + \theta) \right)$$

$$U \frac{\partial \theta}{\partial X} + V \frac{\partial \theta}{\partial Y} = \left(\frac{\partial^2 \theta}{\partial X^2} + \frac{\partial^2 \theta}{\partial Y^2} \right) \tag{10}$$

$$Le \left(U \frac{\partial C}{\partial X} + V \frac{\partial C}{\partial Y} \right) = \left(\frac{\partial^2 C}{\partial X^2} + \frac{\partial^2 C}{\partial Y^2} \right) \tag{11}$$

$$\bar{\mu}_a = \left\{ 2 \left[\left(\frac{\partial U}{\partial X} \right)^2 + \left(\frac{\partial V}{\partial Y} \right)^2 \right] + \left(\frac{\partial V}{\partial X} + \frac{\partial U}{\partial Y} \right)^2 \right\}^{\frac{n-1}{2}}$$

The dimensionless boundary conditions are

1. The conditions at the cold wall are

At $C = 0, \theta = 0$ and $U = V = 0$

2. The conditions at the hot wall are
At $C = 1, \theta = 1$ and $U = V = 0$
3. The conditions at the adiabat walls are
At $C_n = 0, \theta_n = 0, U = V = 0$
The mean Nusselt number is computed thus

$$Nu_{av} = \int_0^1 Nu dY \tag{12}$$

The mean Sherwood Number is computed thus

$$Sh_{av} = \int_0^1 Sh dY \tag{13}$$

The Nusselt number Nu_{10} and Sherwood Number (local) Sh_{10} are computed through the equations.

$$Nu_{10} = -\left(\frac{\partial\theta}{\partial n}\right)_s \tag{14}$$

$$Sh_{10} = -\left(\frac{\partial C}{\partial n}\right)_s \tag{15}$$

In addition, the kinetic energy (total) is

$$K.E. = \frac{1}{2} \int_{\Omega} \|U\|^2 d\Omega \tag{16}$$

Various computational methods have been developed to analyze fluid flow and heat transfer rates within the cavity. This study employs the Finite Element Method (FEM) to discretize and solve Equations (7)–(11) along with their respective boundary conditions. To enhance the precision of the solution, a hybrid mesh combining both triangular and rectangular elements is employed, as illustrated in Figure 2. The simulation is conducted using COMSOL 6.1, a finite element-based software. Table 1 represents the grid convergence study of the simulation, where the number of elements is denoted as NELs, the degrees of freedom are DOFs, and the averaged Nusselt number is denoted as Nu_{avg} . Values are reported for different grid levels. The simulation is conducted using a power law fluid with a shear-thinning behavior, measured by the power law index $n = 0.7, \gamma = 0^\circ, Da = 0.001$, the Hartmann number $Ha = 40$, and the Rayleigh number $Ra = 10^4$. The table shows that as the grid is refined from the extremely coarse level to the extremely fine level, the Nusselt number average value increases gradually. It can be noted that the increase in the Nusselt number average value is relatively small for the finer grid levels, which indicates that the values at the finer level match those at the extra fine level.

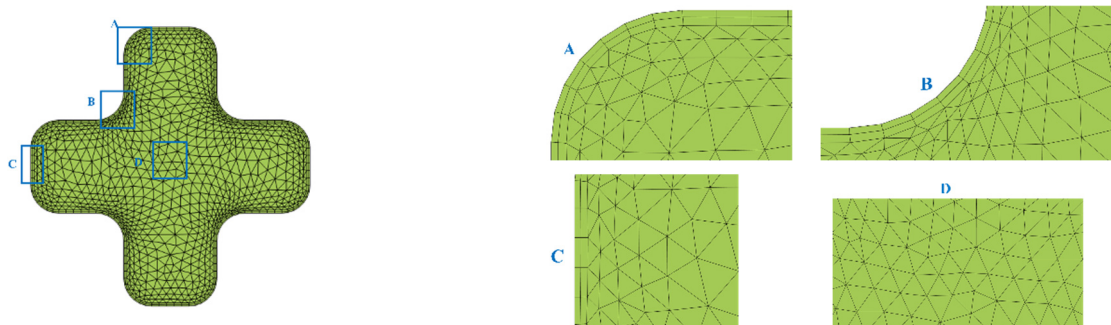


Figure 2. Mesh analysis at an extra fine level is shown in the figure, highlighting the specific mesh region (A–D).

Table 1. Grid independence test for $n = 0.7$, $Ra = 10^4$, $Ha = 20$, $Da = 0.001$, and $\gamma = 0^\circ$.

Level	NELs	DOFs	Nu_{avg}
Extremely coarse	414	3296	0.991965238
Extra coarse	540	4259	1.003046476
Coarser	872	6705	1.007611373
Coarse	1500	11,219	1.013042834
Normal	1558	11,596	1.013021766
Fine	2158	15,784	1.014833783
Finer	4986	35,750	1.020302651
Extra fine	13,800	96,065	1.025686961
Extremely fine	17,104	117,541	1.025693644

The numerical methods used in this study were validated by comparing the results with Khezzar [14] and Bilal [38], who investigated the natural convection of non-Newtonian fluids. The comparison was based on the Nu_{avg} values for various $Pr = 100$, $Ra = 10^3$, and $Ha = 10$. The findings presented in Table 2 demonstrate excellent concurrence between the current results and the available literature data, with a maximum deviation of less than 2.5%. This serves as proof of the exceptional accuracy achieved by the numerical methods employed in this study.

Table 2. Analysis of grid convergence at various refinement levels.

n	Nu_{avg} in [14]	Nu_{avg} in [38]	Present
0.6	6.9345	6.9872	6.9136
0.8	5.5127	5.6200	5.5056
1.0	4.6993	4.6990	4.6810
1.2	3.1709	3.1705	3.1704
1.4	3.7869	3.7870	3.7812

3. Weak Formulation

This section is focused on fundamental aspects of the finite element procedure, encompassing the process of discretizing the governing partial differential equations through a weak formulation. The weak form permits the utilization of lower-degree polynomials for approximating field variables. Fundamentally, the concept of finite element analysis starts by partitioning the bounded domain A into a finite number of smaller, non-overlapping subdomains. Each of these subdomains represents a portion of the primary problem domain. FEM systematically models function spaces within subdomains and approximates functions within each subdomain using piecewise techniques rather than seeking a single function to represent the entire domain. This method generates a series of functions within subdomains intended for approximation within Sobolev test spaces, providing a measure of function smoothness and suitability for solving partial differential equation (PDE) problems. The weak formulation of flows of Bingham-type fluids is discussed in [42], while [43] focuses on laminar, uniform, and incompressible flow, and [40] addresses the power law fluid model. The given expression represents the weak form of Equations (7)–(11), as described in [38,40].

$$\int_A \left(\frac{\partial U}{\partial X} + \frac{\partial V}{\partial Y} \right) w dA = 0 \tag{17}$$

$$\int_A \left(U \frac{\partial U}{\partial X} + V \frac{\partial U}{\partial Y} \right) w dA + \int_A \frac{\partial P}{\partial X} w dA - Pr \int_A \left[2 \frac{\partial}{\partial X} \left(\bar{\mu}_a \left(\frac{\partial U}{\partial X} \right) + \frac{\partial}{\partial Y} \left(\bar{\mu}_a \left(\frac{\partial U}{\partial X} + \frac{\partial V}{\partial X} \right) \right) \right) \right] w dA - \int_A \zeta_X w dA = 0 \tag{18}$$

$$\int_A \left(U \frac{\partial V}{\partial X} + V \frac{\partial U}{\partial Y} \right) w dA + \int_A \frac{\partial P}{\partial Y} w dA - Pr \int_A \left[2 \frac{\partial}{\partial Y} \left(\bar{\mu}_a \left(\frac{\partial V}{\partial Y} \right) + \frac{\partial}{\partial X} \left(\bar{\mu}_a \left(\frac{\partial U}{\partial Y} + \frac{\partial V}{\partial X} \right) \right) \right) \right] w dA - \int_A \zeta_Y w dA = 0 \tag{19}$$

$$\int_A \left(U \frac{\partial \theta}{\partial X} + V \frac{\partial \theta}{\partial Y} \right) w dA - \int_A \left(\frac{\partial^2 \theta}{\partial X^2} + \frac{\partial^2 \theta}{\partial Y^2} \right) w dA = 0 \tag{20}$$

$$\int_A \left(U \frac{\partial C}{\partial X} + V \frac{\partial C}{\partial Y} \right) w dA - \frac{1}{L_e} \int_A \left(\frac{\partial^2 C}{\partial X^2} + \frac{\partial^2 C}{\partial Y^2} \right) w dA = 0 \tag{21}$$

$$\bar{\mu}_a = \int_A \left[2 \left\{ \left(\frac{\partial U}{\partial X} \right)^2 + \left(\frac{\partial V}{\partial X} \right)^2 \right\} + \left(\frac{\partial V}{\partial X} + \frac{\partial U}{\partial Y} \right)^2 \right]^{\frac{n-1}{2}} w dA$$

To achieve a numerical approximation, we evaluate the solutions obtained using both continuous and discrete methods within finite-dimensional subspaces.

$$\left. \begin{aligned} U &\approx U_k \\ V &\approx V_k \\ \theta &\approx \theta_k \end{aligned} \right\} \in w_k, \left. \begin{aligned} C &\approx C_k \in q_k \\ P &\approx P_k \in Q_k \end{aligned} \right\} \tag{22}$$

By substituting Equation (22) into the aforementioned equation, we obtain the discrete version as follows.

$$\int_A \left(\frac{\partial U_k}{\partial X} + \frac{\partial V_k}{\partial Y} \right) w_k dA = 0 \tag{23}$$

$$\int_A \left(U_k \frac{\partial U_k}{\partial X} + V_k \frac{\partial U_k}{\partial Y} \right) w_k dA + \int_A \frac{\partial P_k}{\partial Y} w_k dA - Pr \int_A \left[2 \frac{\partial \bar{\mu}_a}{\partial X} \frac{\partial U_k}{\partial X} + \frac{\partial \bar{\mu}_a}{\partial Y} \left(\frac{\partial^2 U_k}{\partial Y^2} + \frac{\partial^2 V_k}{\partial X \partial Y} \right) \right] w_k dA - \int_A \zeta_X w_k dA = 0 \tag{24}$$

$$\int_A \left(U_k \frac{\partial V_k}{\partial X} + V_k \frac{\partial V_k}{\partial Y} \right) w_k dA + \int_A \frac{\partial P_k}{\partial Y} w_k dA - Pr \int_A \left[2 \frac{\partial \bar{\mu}_a}{\partial Y} \frac{\partial^2 V_k}{\partial Y^2} + \frac{\partial \bar{\mu}_a}{\partial X} \left(\frac{\partial^2 V_k}{\partial X^2} + \frac{\partial^2 U_k}{\partial X \partial Y} \right) \right] w_k dA - \int_A \zeta_Y w_k dA = 0 \tag{25}$$

$$\int_A \left(U_k \frac{\partial \theta_k}{\partial X} + V_k \frac{\partial \theta_k}{\partial Y} \right) w_k dA - \int_A \left(\frac{\partial^2 \theta_k}{\partial X^2} + \frac{\partial^2 \theta_k}{\partial Y^2} \right) w_k dA = 0 \tag{26}$$

$$\int_A \left(U_k \frac{\partial C_k}{\partial X} + V_k \frac{\partial C_k}{\partial Y} \right) w_k dA - \frac{1}{L_e} \int_A \left(\frac{\partial^2 C_k}{\partial X^2} + \frac{\partial^2 C_k}{\partial Y^2} \right) w_k dA = 0 \tag{27}$$

The viscosity relationship for each element in the power law fluid is as defined below.

$$\bar{\mu}_a = \int_A \left[2 \left\{ \left(\frac{\partial U_k}{\partial X} \right)^2 + \left(\frac{\partial V_k}{\partial X} \right)^2 \right\} + \left(\frac{\partial V_k}{\partial X} + \frac{\partial U_k}{\partial Y} \right)^2 \right]^{\frac{n-1}{2}} w dA$$

The discrete solution, in the form of basis functions combined with linear functionals, is as follows.

$$\left. \begin{aligned} U_k &\approx \sum_{h=1}^N U_h \phi_h(x, y) \\ V_k &\approx \sum_{h=1}^N V_h \phi_h(x, y) \\ P_k &\approx \sum_{h=1}^N P_h \Psi_h(x, y) \end{aligned} \right\} \left. \begin{aligned} \theta_k &\approx \sum_{h=1}^N \theta_h \theta_h(x, y) \\ C_k &\approx \sum_{h=1}^N C_h C_h(x, y) \end{aligned} \right\} \tag{28}$$

The continuity equation, momentum, energy, and concentration at the element level for n degrees of freedom is

$$\int_A \left(\frac{\partial U_k}{\partial X} + \frac{\partial V_k}{\partial Y} \right) w_k dA = 0 \tag{29}$$

$$\int_A \left(U_k \frac{\partial U_k}{\partial X} + V_k \frac{\partial U_k}{\partial Y} \right) w_k dA + \int_A \frac{\partial P_k}{\partial X} w_k dA - Pr \int_A \left[2 \frac{\partial \bar{\mu}_a}{\partial X} \frac{\partial U_k}{\partial X} \frac{\partial w_k}{\partial X} + \frac{\partial \bar{\mu}_a}{\partial Y} \left(\frac{\partial^2 U_k}{\partial Y^2} \frac{\partial^2 w_k}{\partial Y^2} + \frac{\partial^2 V_k}{\partial Y \partial X} \frac{\partial^2 w_k}{\partial Y \partial X} \right) \right] dA - \int_A \zeta_X w_k dA = 0 \tag{30}$$

$$\int_A \left(U_k \frac{\partial V_k}{\partial X} + V_k \frac{\partial V_k}{\partial Y} \right) w_k dA + \int_A \frac{\partial P_k}{\partial Y} w_k dA - Pr \int_A \left[2 \frac{\partial \bar{\mu}_a}{\partial Y} \frac{\partial^2 V_k}{\partial Y^2} \frac{\partial^2 w_k}{\partial Y^2} + \frac{\partial \bar{\mu}_a}{\partial X} \left(\frac{\partial^2 U_k}{\partial X \partial Y} \frac{\partial^2 w_k}{\partial X \partial Y} + \frac{\partial^2 V_k}{\partial X^2} \frac{\partial^2 w_k}{\partial X^2} \right) \right] dA - \int_A \zeta_Y w_k dA = 0 \tag{31}$$

$$\int_A \left(U_k \frac{\partial \theta_k}{\partial X} + V_k \frac{\partial \theta_k}{\partial Y} \right) w_k dA + \int_A \left(\frac{\partial \theta_k}{\partial X} \frac{\partial w_k}{\partial X} + \frac{\partial \theta_k}{\partial Y} \frac{\partial w_k}{\partial Y} \right) dA = 0 \tag{32}$$

$$\int_A \left(U_k \frac{\partial C_k}{\partial X} + V_k \frac{\partial C_k}{\partial Y} \right) w_k dA - \frac{1}{Le} \int_A \left(\frac{\partial C_k}{\partial X} \frac{\partial w_k}{\partial X} + \frac{\partial C_k}{\partial Y} \frac{\partial w_k}{\partial Y} \right) dA = 0 \tag{33}$$

The parameters maintain their standard definitions, and the solution is obtained by iteratively processing the non-linear system until a specific value is achieved.

4. Results and Discussions

The study utilized the finite element method to investigate the heat transfer properties of a power law fluid contained within a plus-shaped enclosure. The analysis meticulously examined variations in velocity and temperature distribution in relation to distinct magnitudes of crucial parameters, such as the Prandtl number Pr , the power law index n , and the Rayleigh number Ra . This method facilitated a comprehensive understanding of the complex interplay between different factors and their impact on the fluid’s behavior. Moreover, the study also calculated local and mean heat transfer rates and K.E. measurements related to various variables. The fluctuations in Nu concerning the power law fluid n are presented in Table 2 for a comprehensive understanding of their relationship. The analysis demonstrates that when the power law index n increases, a simultaneous decline is observed in heat transfer. This is attributed to the fluid’s behavior transitioning from pseudoplastic to dilatant as the power law index increases. Hence, the increase in fluid viscosity as an effect contributes to reducing the motion and heat transfer processes within the flow domain.

In Figure 3 with $Ha = 0$, it has been found that the enclosure is primarily occupied by a single convective cell, which is aligned diagonally within the enclosure. The fluid moves near the walls, while the temperature moves closer to the central point. The diagonal walls are considered to be adiabatic. This leads to the formation of a counterclockwise flow pattern within the cavity. When Darcy’s number rises $10^{-4} \leq Da \leq 10^{-2}$, the main convective cell expands horizontally, and secondary cells emerge in opposite corners, reflecting a stronger convective process within the enclosure. Moreover, an increase in the Da leads to higher stream function values, signifying a notable impact on fluid movement within the cavity. The results show that as Da increases, there is a decrease in fluid resistance inside the cavity, which, in turn, leads to a considerable enhancement in convective fluid intensity. As a result, the fluid flow properties are positively influenced by the Da number, improving the overall behavior of the fluid within the cavity.

Figure 4 illustrates the changes in temperature distribution as the Darcy number increases, which is associated with the consistent heating applied to the side walls. When $Ha = 0$ and all evaluated power law indices and isotherm lines parallel to vertical walls are noticeable at a low Darcy number $Da = 10^{-4}$, this indicates that conduction is the dominant mode of heat transfer in this case. As the Darcy number increases, heat transfer diagonally from right to left walls occurs more rapidly, owing to the enhanced convective flow within the enclosure. The thermal gradients surrounding the vertical side walls are considerably steeper than those observed at the lower Darcy number. As the Ha number increases, its impact on isotherms indicates a substantial reduction in the thermal convection effect. At low Ha numbers, conduction is the main mode of heat transfer, causing the temperature distribution to be less influenced by the applied magnetic field.

Moreover, when Da (ranging from low to high) and the Ha number increase, the isotherms are adversely affected, resulting in the restraint of convective flow within the enclosure.

Figure 5 demonstrates the impact of different Rayleigh numbers $10^4 \leq Ra \leq 10^6$ and Hartmann numbers $Ha = 0, 40$ on the streamlines within the cavity for two different rheological behaviors of the fluid, $n = 0.7$ (shear-thinning behavior) and $n = 1.2$ (shear-thickening behavior). When $Ha = 0$, the discussion primarily centered around the influence of Ra and fluid rheology on the streamlines inside the cavity. The results showed that for both the pseudoplastic behavior $n = 0.7$ and dilatant behavior $n = 1.2$ fluids, as the Ra increased from 10^4 to 10^6 the fluid motion became more ordered and stable. The streamlines became more twisted on the vertical side, and the convective cells in the bottom right and upper left corners became more noticeable. For the pseudoplastic behavior of the fluid, the fluid velocity increased significantly, and the fluid moved in a more circular motion, while for the shear-thickening fluid, the velocity decreased slightly, and the fluid moved in a more linear motion.

The behavior of the fluid is significantly influenced by the presence of a magnetic field, particularly for the maximum value of the Hartmann number. The fluid's flow became more regular and steadier in the presence of the magnetic field, resulting in weaker and less intense convective cells within the enclosure. In the case of the shear-thinning fluid, the impact of the Rayleigh number Ra and the rheological attributes on the streamlines was insignificant. A rise in Rayleigh number for shear-thickening fluid resulted in more vertically elongated streamlines. The convective cells in the lower and upper corners became more pronounced and distinct.

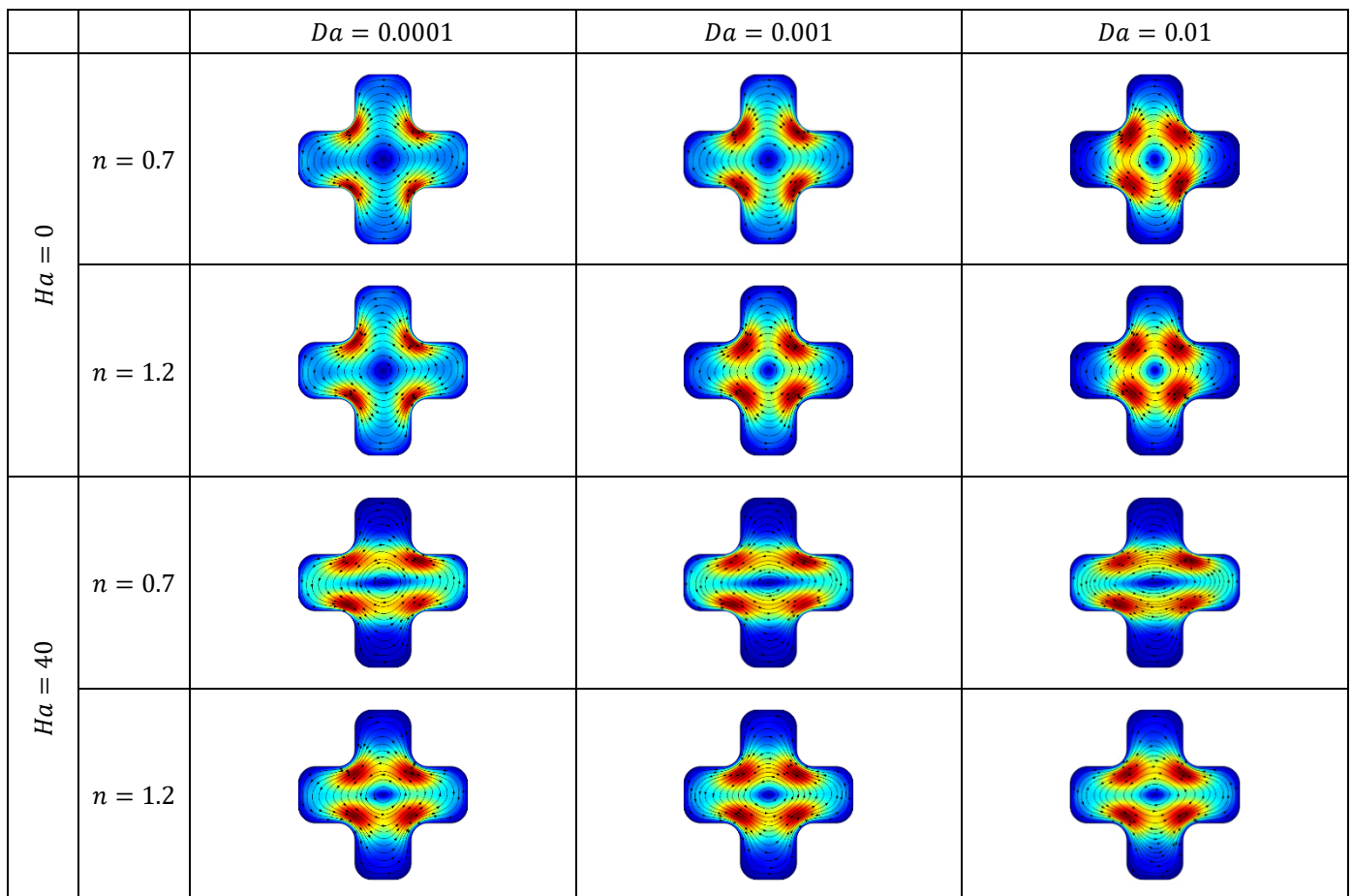


Figure 3. Variation of streamlines with Ha , Da , and n values at specified parameters of $Ra = 10^4$, $Pr = 0.7$, and $\gamma = 0^\circ$.

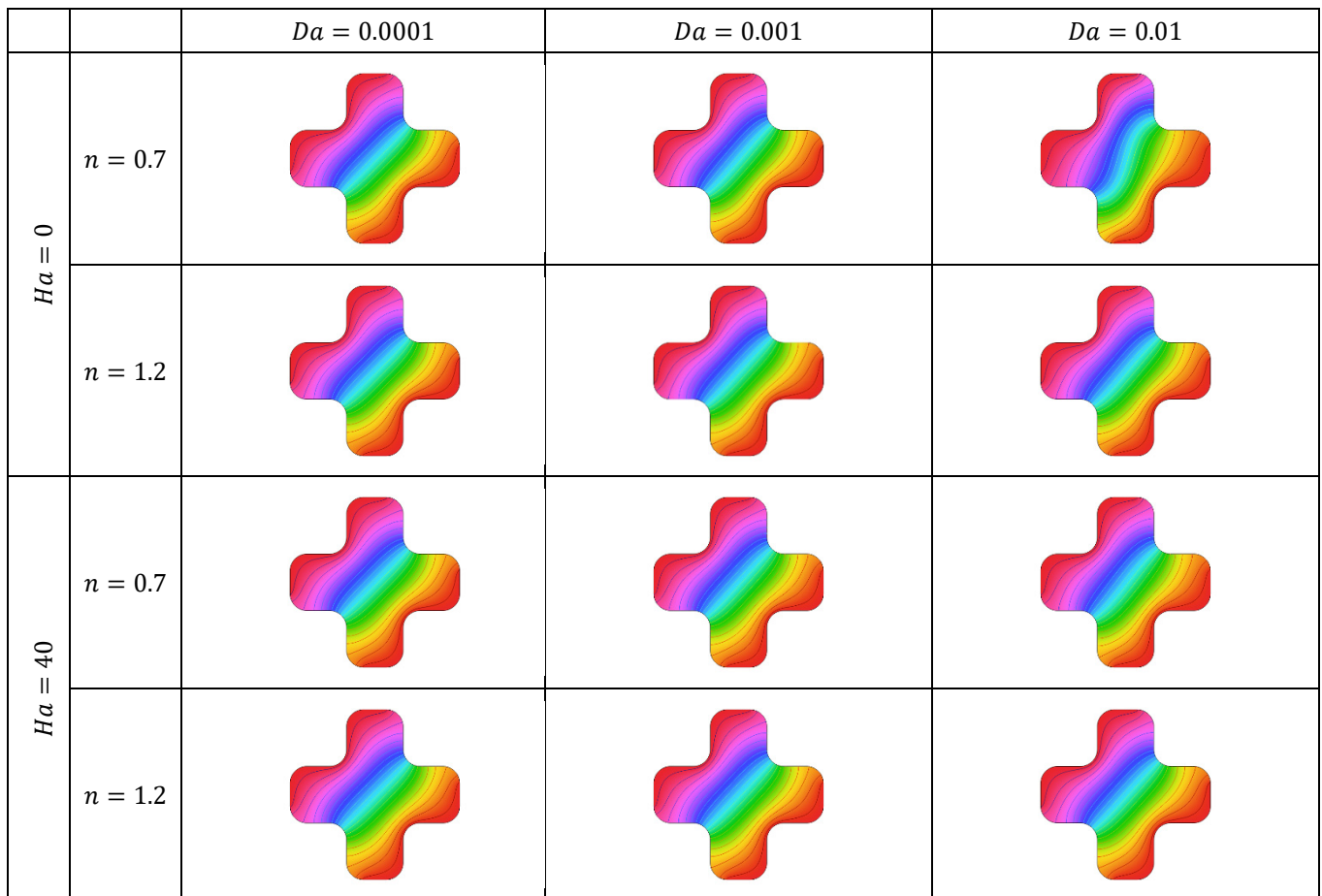


Figure 4. Variation of isotherms with Ha , Da , and n values at specified parameters of $Ra = 10^4$, $Pr = 0.7$, and $\gamma = 0^\circ$.

The impact of kinetic energy at power law indices n and various Rayleigh numbers Ra is presented in Table 3. The kinetic energy is calculated based on the FEM simulations conducted in the study. The results show that the kinetic energy escalates with an increase in the Ra . Moreover, $n = 0.7$ (shear-thinning fluid) exhibits higher kinetic energy values as compared to the shear-thickening fluid $n = 1.2$ and Newtonian fluid $n = 1$ for all evaluated Ra values, indicating better fluid motion and convective heat transfer.

Table 3. Comparison of kinetic Energy for different n and Ra .

Rayleigh Number Ra	Shear-Thinning $n = 0.7$	Newtonian $n = 1$	Shear-Thickening $n = 1.2$
1000	0.000604989	0.000506759	0.000457145
10,000	0.088720673	0.054054614	0.035492132
100,000	20.27295603	8.693457243	3.339311009
1,000,000	763.1102155	485.2226004	155.4152072

Figure 6 represents the influence of Ra on the isotherms within the cavity for two different rheological behaviors of the fluid, shear-thickening and shear-thinning while keeping the Hartmann number $Ha = 0$. For the shear-thinning fluid $n = 0.7$, at low Rayleigh number $Ra = 10^4$, the temperature distribution is dominated by conduction, and the isotherms are along the vertical walls. With an increase in the Ra , the isotherms become more prolonged, indicating the onset of convection. At higher Rayleigh numbers $Ra = 10^6$, the isotherms become more irregular, indicating strong convection within the enclosure. For the shear-thickening fluid $n = 1.2$, the impact of the Rayleigh number on

the isotherms is similar, but the overall temperature distribution is less affected compared to the shear-thinning fluid.

For a fixed Hartmann number of 40 and a varying Rayleigh number ranging from 10^4 to 10^6 , significant changes in the cavity's isotherms are observed for pseudoplastic behavior $n = 0.7$ and dilatant behavior $n = 1.2$ fluids. With an increase in the Rayleigh number, the isotherms for $n = 0.7$ exhibit slight distortion, resulting in a more pronounced temperature gradient along the side walls of the enclosure. When $n = 1.2$, the Rayleigh number increases because of thermal distribution, resulting in an overall decrease in the temperature gradient. When Ra increases, several changes occur in the isotherms within the cavity. Specifically, the thermal gradient is more prominent in the case of the pseudoplastic behavior as compared to the dilatant behavior fluid.

Table 4 presents the variation of the Nusselt number across various Hartmann numbers, the power law index n , and the Darcy numbers. The outcomes indicate that the heat transfer rate increases when the Hartmann number increases for all values of n and the Darcy numbers. Similarly, when the Darcy number increases, the heat transfer rate increases for all power law exponent n and Hartmann number values. The results also indicate that the Nu_{avg} has a maximum value for lower values of n (power law exponent).

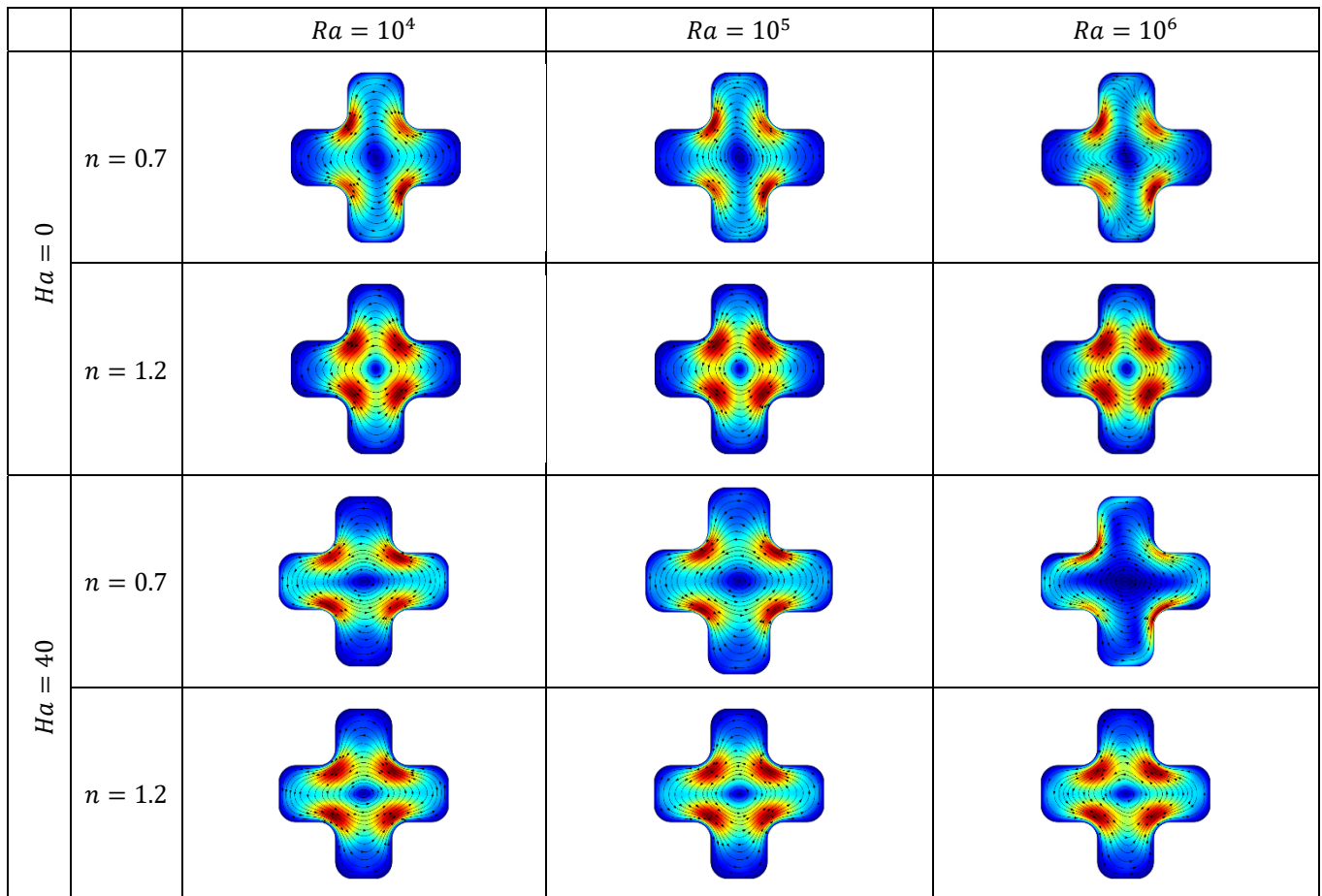


Figure 5. Variation of streamlines with Ra , Ha , and n values at specified parameters of $Da = 0.001$, $Pr = 0.7$, and $\gamma = 0^\circ$.

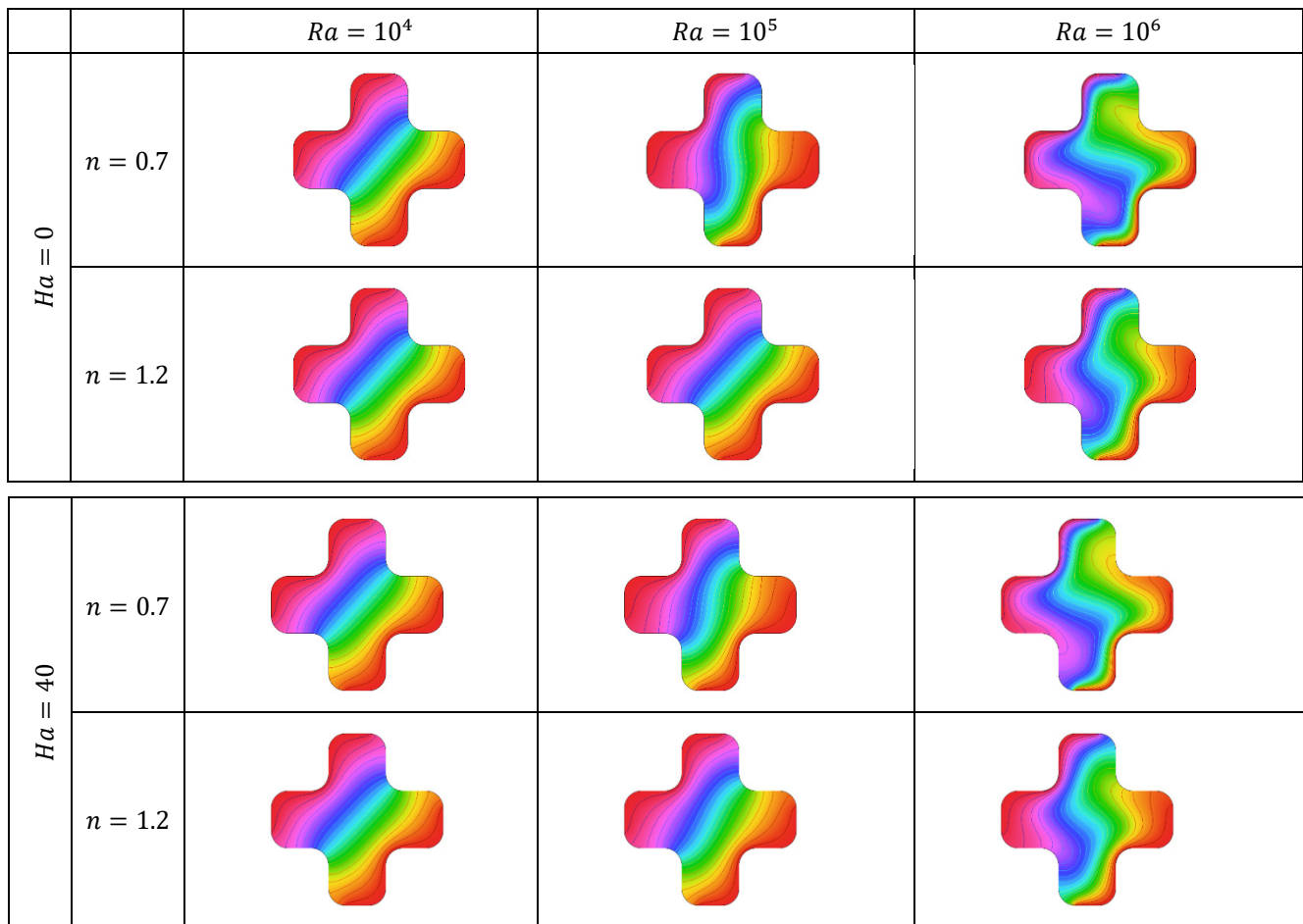


Figure 6. Variation of isotherms with Ra , Ha , and n values at specified parameters of $Da = 0.001$, $Pr = 0.7$, and $\gamma = 0^\circ$.

Table 4. Variation of Nusselt numbers for different Hartmann numbers, Darcy numbers and power law index n .

Da	$Ha=0$			$Ha=20$			$Ha=40$		
	10^{-4}	10^{-3}	10^{-2}	10^{-4}	10^{-3}	10^{-2}	10^{-4}	10^{-3}	10^{-2}
n									
0.7	1.022770	1.025936	1.137129	1.02277	1.025153	1.052084	1.022768	1.024156	1.030507
1	1.022764	1.024352	1.033057	1.022763	1.024044	1.028685	1.022762	1.023584	1.025327
1.2	1.022758	1.023468	1.024544	1.022758	1.023375	1.024198	1.022756	1.023203	1.023664
1.6	1.022753	1.023081	1.023303	1.022753	1.023054	1.023249	1.022752	1.022994	1.023134

The line graph in Figure 7 illustrates the impact of the Hartmann number Ha , Kinetic energy, and heat transfer rate for two different rheological behaviors of the fluid, shear-thickening and shear-thinning, at different angles of inclination (0° , 30° , and 60°). For shear-thinning fluid $n = 0.7$, as the Hartmann number Ha increases from 0 to 40, the averaged Nusselt number decreases for all angles of inclination (0° , 30° , and 60°), with the same behavior for kinetic energy. When $Ha = 0$, the averaged Nusselt number and kinetic energy have maximum value. With the increase in Ha , the heat transfer rate and kinetic energy decrease. Moreover, the influence of the degree of inclination can be noticed with the 0° inclination having the greatest Nusselt number, followed by 30° and 60° . For shear-thickening fluids $n = 1.2$, similar to shear-thinning fluids, the averaged Nusselt number decreases as the Hartmann number Ha increases from 0 to 40, irrespective of the inclination angle. The different angles of inclination, the 0° angle generally results in the highest

Nusselt number. It can be concluded that shear-thinning and shear-thickening fluids are consistent regarding the effect of Hartmann number Ha on the averaged Nusselt number. As Ha increases, the Nusselt number decreases, indicating a reduction in convective heat transfer. The results show that the magnetic field-induced flow suppression has a substantial impact on the kinetic energy within the cavity, particularly for shear-thinning behavior.

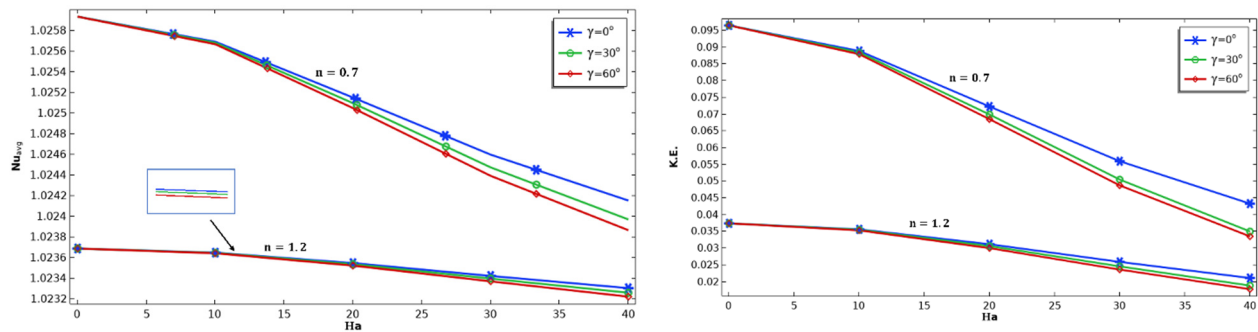


Figure 7. Variation of averaged Nusselt number for different values of inclined angle γ at specified parameters of $Da = 0.001$, $Pr = 0.7$, $Ra = 10^4$, and $\gamma = 0^\circ$.

5. Conclusions

The primary aim of this study is to conduct a thorough exploration of the thermal characteristics of power law liquid flow within a plus-shaped enclosure under conditions of natural convection. The analysis includes significant parameters and utilizes the finite element method (FEM) to investigate the heat transfer characteristics of the fluid. Results showed fluid behavior and the intricate interaction between important parameters like the Rayleigh number (Ra), the power law index (n), and the Prandtl number (Pr), which affect velocity and temperature distribution. Different variables were considered for measuring kinetic energy and heat transfer rates. The results showed that both the kinetic energy and the heat transfer rate increased when the Rayleigh number increased. The Nusselt number is higher for the shear-thinning case ($n = 0.7$) compared to Newtonian ($n = 1$) and shear-thickening cases ($n = 1.2$). When the Rayleigh number (Ra) increases, the heat transfer rate in the flow domain also increases due to the temperature difference. For a higher value of Darcy number, (Da) and (Ha) have a favorable impact on the fluid behavior within the cavity, leading to a greater intensity of convective fluid. The results of this investigation provide significant information for optimizing the design of a plus-shaped cavity for power law fluids, which is essential for effective heat transfer systems, contributing to the advancement of design strategies in this field.

Author Contributions: Conceptualization, I.S.C.; methodology, I.S.C.; software, I.S.C. and M.Y.; validation, I.S.C., J.L. and M.A.M.; formal analysis, I.S.C. and M.Y.; investigation, I.S.C. and Z.G.; writing—original draft preparation, I.S.C.; writing—review and editing, I.S.C., J.L. and Z.G.; supervision, J.L.; funding acquisition, J.L. All authors have read and agreed to the published version of the manuscript.

Funding: This research was supported by the National Natural Science Foundation of China (grant no. 12272011) and also supported by the National Key R&D Program of China (grant no. 2022YFB3806000).

Institutional Review Board Statement: Not applicable.

Informed Consent Statement: Not applicable.

Data Availability Statement: Not applicable.

Conflicts of Interest: The authors declare no conflict of interest.

References

1. Cesini, G.; Paroncini, M.; Cortella, G.; Manzan, M. Natural convection from a horizontal cylinder in a rectangular cavity. *Int. J. Heat Mass Transf.* **1999**, *42*, 1801–1811. [[CrossRef](#)]
2. Roychowdhury, D.; Das, S.K.; Sundararajan, T. Numerical simulation of natural convective heat transfer and fluid flow around a heated cylinder inside an enclosure. *Heat Mass Transf.* **2002**, *38*, 565–576. [[CrossRef](#)]
3. Angeli, D.; Levoni, P.; Barozzi, G.S. Numerical predictions for stable buoyant regimes within a square cavity containing a heated horizontal cylinder. *Int. J. Heat Mass Transf.* **2008**, *51*, 553–565. [[CrossRef](#)]
4. Bouafia, M.; Daube, O. Natural convection for large temperature gradients around a square solid body within a rectangular cavity. *Int. J. Heat Mass Transf.* **2007**, *50*, 3599–3615. [[CrossRef](#)]
5. Butler, C.; Newport, D.; Geron, M. Natural convection experiments on a heated horizontal cylinder in a differentially heated square cavity. *Exp. Therm. Fluid Sci.* **2013**, *44*, 199–208. [[CrossRef](#)]
6. Pandey, S.; Park, Y.G.; Ha, M.Y. An exhaustive review of studies on natural convection in enclosures with and without internal bodies of various shapes. *Int. J. Heat Mass Transf.* **2019**, *138*, 762–795. [[CrossRef](#)]
7. Ostrach, S. Natural convection in enclosures. *J. Heat Transfer.* **1988**, *110*, 1175–1190. [[CrossRef](#)]
8. Hajmohammadi, M.; Rahmani, M.; Campo, A.; Shariatzadeh, O.J. Optimal design of unequal heat flux elements for optimized heat transfer inside a rectangular duct. *Energy* **2014**, *68*, 609–616. [[CrossRef](#)]
9. Kwon, H.; Joo, Y.; Kim, S.J. Analytic approach to thermal optimization of horizontally oriented radial plate-fin heat sinks in natural convection. *Energy Convers. Manag.* **2018**, *156*, 555–567. [[CrossRef](#)]
10. Schaub, M.; Kriegel, M.; Brandt, S. Analytical prediction of heat transfer by unsteady natural convection at vertical flat plates in air. *Int. J. Heat Mass Transf.* **2019**, *144*, 118665. [[CrossRef](#)]
11. Ahn, C.-S.; Bang, B.-H.; Park, C.; Kim, D.-Y.; Yarin, A.L.; Yoon, S.S. Experimental, analytical, and computational study of natural convection in asymmetrically-heated vertical shafts. *Int. J. Therm. Sci.* **2021**, *170*, 107131. [[CrossRef](#)]
12. Malkeson, S.; Alshaaaili, S.; Chakraborty, N. Numerical investigation of steady state laminar natural convection of power-law fluids in side-cooled trapezoidal enclosures heated from the bottom. *Numer. Heat Transf. Part A* **2023**, *83*, 770–789. [[CrossRef](#)]
13. Alloui, Z.; Khelifa, N.B.; Beji, H.; Vasseur, P.; Guizani, A. The onset of convection of power-law fluids in a shallow cavity heated from below by a constant heat flux. *J. Non-Newton. Fluid Mech.* **2013**, *196*, 70–82. [[CrossRef](#)]
14. Khezzar, L.; Siginer, D.; Vinogradov, I. Natural convection of power law fluids in inclined cavities. *Int. J. Therm. Sci.* **2012**, *53*, 8–17. [[CrossRef](#)]
15. Sairamu, M.; Chhabra, R. Natural convection in power-law fluids from a tilted square in an enclosure. *Int. J. Heat Mass Transf.* **2013**, *56*, 319–339. [[CrossRef](#)]
16. Mishra, L.; Chhabra, R.P. Natural convection in power-law fluids in a square enclosure from two differentially heated horizontal cylinders. *Heat Transf. Eng.* **2018**, *39*, 819–842. [[CrossRef](#)]
17. Berrehal, H.; Dinarvand, S.; Khan, I. Mass-based hybrid nanofluid model for entropy generation analysis of flow upon a convectively-warmed moving wedge. *Chin. J. Phys.* **2022**, *77*, 2603–2616. [[CrossRef](#)]
18. Wakif, A.; Shah, N.A. Hydrothermal and mass impacts of azimuthal and transverse components of Lorentz forces on reacting Von Kármán nanofluid flows considering zero mass flux and convective heating conditions. *Waves Random Complex Media* **2022**, 1–22. [[CrossRef](#)]
19. Ananth Subray, P.V.; Hanumagowda, B.N.; Varma, S.V.K.; Zidan, A.M.; Kbiri Alaoui, M.; Raju, C.S.K.; Shah, N.A.; Junsawang, P. Dynamics of Heat Transfer Analysis of Convective-Radiative Fins with Variable Thermal Conductivity and Heat Generation: Differential Transformation Method. *Mathematics* **2022**, *10*, 3814. [[CrossRef](#)]
20. Sandeep, N.; Sulochana, C. Momentum and heat transfer behaviour of Jeffrey, Maxwell and Oldroyd-B nanofluids past a stretching surface with non-uniform heat source/sink. *Ain Shams Eng. J.* **2018**, *9*, 517–524. [[CrossRef](#)]
21. Ramesh, G.; Madhukesh, J.; Shah, N.A.; Yook, S.-J. Flow of hybrid CNTs past a rotating sphere subjected to thermal radiation and thermophoretic particle deposition. *Alex. Eng. J.* **2023**, *64*, 969–979. [[CrossRef](#)]
22. Bilal, S.; Khan, N.Z.; Fatima, I.; Riaz, A.; Ansari, G.J.; Alhazmi, S.E.; El-Din, E.M. Mixed convective heat transfer in a power-law fluid in a square enclosure: Higher order finite element solutions. *Front. Phys.* **2023**, *10*, 1327. [[CrossRef](#)]
23. Dinarvand, S.; Nejad, A.M. Off-centered stagnation point flow of an experimental-based hybrid nanofluid impinging to a spinning disk with low to high non-alignments. *Int. J. Numer. Methods Heat Fluid Flow* **2021**, *32*, 2799–2818. [[CrossRef](#)]
24. Khan, Y.; Majeed, A.H.; Shahzad, H.; Awan, F.J.; Iqbal, K.; Ajmal, M.; Faraz, N. Numerical Computations of Non-Newtonian Fluid Flow in Hexagonal Cavity With a Square Obstacle: A Hybrid Mesh-Based Study. *Front. Phys.* **2022**, *10*, 891163. [[CrossRef](#)]
25. Pirmohammadi, M.; Ghassemi, M. Effect of magnetic field on convection heat transfer inside a tilted square enclosure. *Int. Commun. Heat Mass Transf.* **2009**, *36*, 776–780. [[CrossRef](#)]
26. Hussain, S.; Jamal, M.; Haddad, Z.; Arıcı, M. Numerical modeling of magnetohydrodynamic thermosolutal free convection of power law fluids in a staggered porous enclosure. *Sustain. Energy Technol. Assess.* **2022**, *53*, 102395. [[CrossRef](#)]
27. Raizah, Z.; Aly, A.M.; Ahmed, S.E. Natural convection flow of a power-law non-Newtonian nanofluid in inclined open shallow cavities filled with porous media. *Int. J. Mech. Sci.* **2018**, *140*, 376–393. [[CrossRef](#)]
28. Shah, J.; Ali, F.; Khan, N.; Ahmad, Z.; Murtaza, S.; Khan, I.; Mahmoud, O. MHD flow of time-fractional Casson nanofluid using generalized Fourier and Fick's laws over an inclined channel with applications of gold nanoparticles. *Sci. Rep.* **2022**, *12*, 17364. [[CrossRef](#)]

29. Sheremet, M.A.; Oztop, H.; Pop, I.; Al-Salem, K. MHD free convection in a wavy open porous tall cavity filled with nanofluids under an effect of corner heater. *Int. J. Heat Mass Transf.* **2016**, *103*, 955–964. [[CrossRef](#)]
30. Hussain, S.; Jamal, M.; Geridonmez, B.P. Impact of power law fluid and magnetic field on double diffusive mixed convection in staggered porous cavity considering Dufour and Soret effects. *Int. Commun. Heat Mass Transf.* **2021**, *121*, 105075. [[CrossRef](#)]
31. Yazdani, K.; Sahebjamei, M.; Ahmadpour, A. Natural convection heat transfer and entropy generation in a porous trapezoidal enclosure saturated with power-law non-Newtonian fluids. *Heat Transf. Eng.* **2020**, *41*, 982–1001. [[CrossRef](#)]
32. Daneshvar Garmroodi, M.; Ahmadpour, A.; Hajmohammadi, M.; Gholamrezaie, S. Natural convection of a non-Newtonian ferrofluid in a porous elliptical enclosure in the presence of a non-uniform magnetic field. *J. Therm. Anal. Calorim.* **2020**, *141*, 2127–2143. [[CrossRef](#)]
33. Misirlioglu, A.; Baytas, A.C.; Pop, I. Free convection in a wavy cavity filled with a porous medium. *Int. J. Heat Mass Transf.* **2005**, *48*, 1840–1850. [[CrossRef](#)]
34. Haq, R.U.; Soomro, F.A.; Mekkaoui, T.; Al-Mdallal, Q.M. MHD natural convection flow enclosure in a corrugated cavity filled with a porous medium. *Int. J. Heat Mass Transf.* **2018**, *121*, 1168–1178. [[CrossRef](#)]
35. Giga, Y.; Novotný, A. *Handbook of Mathematical Analysis in Mechanics of Viscous Fluids*; Springer: Berlin/Heidelberg, Germany, 2018.
36. Litvinov, V.G. *Motion of a Nonlinear-Viscous Fluid*; Nauka: Moscow, Russia, 1982; Volume 210.
37. Baranovskii, E.S.; Artemov, M.A. Existence of optimal control for a nonlinear-viscous fluid model. *Int. J. Differ. Equ.* **2016**, *2016*, 9428128. [[CrossRef](#)]
38. Bilal, S.; Khan, N.Z.; Shah, I.A.; Awrejcewicz, J.; Akgül, A.; Riaz, M.B. Numerical study of natural convection of power law fluid in a square cavity fitted with a uniformly heated T-fin. *Mathematics* **2022**, *10*, 342. [[CrossRef](#)]
39. Kefayati, G. Simulation of double diffusive MHD (magnetohydrodynamic) natural convection and entropy generation in an open cavity filled with power-law fluids in the presence of Soret and Dufour effects (Part II: Entropy generation). *Energy* **2016**, *107*, 917–959. [[CrossRef](#)]
40. Hussain, S.; Öztop, H.F. Impact of inclined magnetic field and power law fluid on double diffusive mixed convection in lid-driven curvilinear cavity. *Int. Commun. Heat Mass Transf.* **2021**, *127*, 105549. [[CrossRef](#)]
41. Kolsi, L.; Hussain, S.; Ghachem, K.; Jamal, M.; Maatki, C. Double diffusive natural convection in a square cavity filled with a porous media and a power law fluid separated by a wavy interface. *Mathematics* **2022**, *10*, 1060. [[CrossRef](#)]
42. Baranovskii, E.S. On flows of Bingham-type fluids with threshold slippage. *Adv. Math. Phys.* **2017**, *2017*, 7548328. [[CrossRef](#)]
43. Aslam, M.A.; Yao, H.; Chuhan, I.S.; Shahzad, H. Finite element modeling of dual convection in a Y shaped porous cavity containing viscous fluid. *Front. Phys.* **2023**, *11*, 1207462. [[CrossRef](#)]

Disclaimer/Publisher's Note: The statements, opinions and data contained in all publications are solely those of the individual author(s) and contributor(s) and not of MDPI and/or the editor(s). MDPI and/or the editor(s) disclaim responsibility for any injury to people or property resulting from any ideas, methods, instructions or products referred to in the content.